Scientific
Research
Publishing

Characterization of Spatio-Temporal Variability of Irradiation, Nebulosity and Aerosols Optical Depth in 10° North-20° North African Band

Abdoulaye Bouya Diop[1], Abdoulaye Sy[1,2], Malick Wade[1], Abdoul Karim Mbodj[1], Abdou Karim Farota[1], Adoum Mahamat Moussa[1,3], Babacar Niang[1], Aicha Dia Diop[1], Bara Ndiaye[1], Bouya Diop[1*] , Amadou Thierno Gaye[4], Aboubakary Diakhaby[1]

[1]LSAO-MED Gaston Berger University, Saint Louis, Senegal
[2]CERDI Clermont Auvergne University, Clermont Auvergne, France
[3]University of Tchad, Djamena, Tchad
[4]LPAOSF ESP Cheikh Anta Diop Univesity, Dakar, Senegal
Email: *bouyadiop@gmail.com

Abstract

This work concerns the 10° North, 20° North African band. Area renowned for having some of the poorest countries in the world. It is also home to the Sahelian strip and part of the Sahara. The countries in this zone have a relatively low electrification rate compared to the enlightened country. To solve this problem, these countries want to turn to renewable energies such as photovoltaics (renewable energy obtained through solar radiation). Therefore, understanding the behavior of irradiation and cloudiness in the 10 - 20 band becomes necessary. The application of the empirical orthogonal functions to the different cloud layers and to the irradiation reveals a seasonality of the latter, in particular compared to the first modes of the empirical orthogonal functions (EOF1). Indeed, by filtering in time and space to isolate solar radiation and cloudiness, the EOF1 expresses respectively 94.3% of the variation of descending solar radiation in clear sky in the 10 - 20 band. Note 65.7% for global radiation, 54.4% for cloudiness at 450 hPa, 69.6% for cloudiness between 800 hPa and 450 hPa, 76.6% for low cloudiness, 61.4% for total cloudiness. These results allow us to say that we have generally good sunshine over several months, with little cloud cover in this band. However, since this zone is considered to be part of the main aerosol emission source zones, it is important in their temporal consideration of the optical depth. By doing the wavelet analysis on the optical depth data from Dakar and Banizoumbou, we note that the average dust presence spectrum over the entire period from

1997 to 2019 in the two stations with a slight shift compared to the peaks and the maximum observed value. A sign that there is a strong presence of dust in this area and that it should be taken into account for any photovoltaic installation in this area.

Keywords

1. Introduction

The long drought from 1970 to 1990 (Nouaceur & Zeineddine, 2020) was caused by a rainfall deficit of 50% to 60% (Paturel, Servat, Delatre, & Lubes-niel, 1998), associated with global warming (Diawara et al., 2021), advance of the desert (Taïbi, 2017), low high vegetation cover (Marega, Emeterio, Fall, & Andrieu, 2021; Emeterio, Lacaze, & Méring, 2012). Makes the Sahelian climate increasingly arid, leading to the appearance of more and more frequent episodes of dust (Nouaceur, 2004). This dust (fine particles or aerosols) has a health (Martiny, Roucou, & Adde, 2014), ecological (Sicard, 1992), environmental, but also climatic impact.

In this work we are interested in the 10˚ North-20˚ North African band (10 - 20 band) delimited by the African continental shelf. This area is the scene of climatic instability, caused by superposition of four types of climates. There are Saharan, Sahelian, Sahelo-Sudanian, Sudano-Sahelian climates, as well as forest areas and flows of desert dust deposits which are the result of the intensity of wind erosion in the Sahelo-Saharan zone (deMenocal & Ortiz, 2000).

Parameters related to uplift, transport and deposition of fine particles (dust) in the 10 - 20 band are related to solar radiation and cloud cover (cloudiness). Indeed, these two parameters play an important role in the temperature gradients, essential factors of all the mechanisms of the circulation of atmospheric dynamics (Deremble, 2010).

To highlight the potential of the 10 - 20 band to receive photovoltaics and the relevance of studying the impact of dust on the latter. We will first study the seasonality of irradiation and nebulosity in the 10 - 20 band from 1980 to 2010 both from a spatial and temporal point of view through empirical orthogonal functions. Subsequently, the behavior of optical depth in the Dakar and Banizoumbou station from 1997 to 2019 will be discussed using wavelet analysis.

2. Data and Methods

In this work we use AOD (Aerosols Optical Depth) optical depth data, as well as irradiation and cloudiness data. These aim to study the variability of intra-annual irradiation and nebulosity as well as their inter-annual seasonalities in the 10 - 20 band. As for the observation of the AOD on Dakar and Banizoumbou, it will edify us on the importance of the presence of aerosol in this zone. These studies

are part of a process of determining the importance of installing photovoltaic solar collectors in the 10 - 20 band. Using solar potential, cloud cover and aerosols, we study the yields of solar collectors. The occasional observation data (Dakar, Banizoumbou) are provided by AERONET (Aerosol Robotic Network) which is a ground aerosol measurement network established by NASA and PHOTONS (PHotometry for Operational Processing of Satellite Normalization, CNES and of CNRS-INSU). This network is greatly enriched by others (RIMA, AeroSpan, AEROCAN and CARSNET) and collaborators from national agencies, institutes, universities, individual scientists and partners. For more than 25 years, the project has provided a long-term, continuous database. This base is easily accessible. It provides information on the optical, microphysical and radiative properties of aerosols. It allows research into the characterization of aerosols. It also allows the validation of satellite extractions and synergy with other databases. The network requires standardization of instruments, calibration, processing and distribution. The AERONET data used here includes optical measurements, providing information on the quantities and properties of aerosols contained in the entire atmospheric column (Rajot et al., 2011). These data are also used in the AMMA project. These data are available on the https://aeronet.gsfc.nasa.gov/platform.

Solar irradiation and specific cloudiness data are directly extracted from the ERA5 platform. ERA5 is the fifth generation of ECMWF reanalysis for global climate and weather for the past 4 - 7 decades. Currently, data from 1979 to present is available. ERA5 replaces ERA-Interim reanalysis (Olauson, 2018; Wang, Graham, Wang, Gerland, & Granskog, 2019). Data were regridded to a regular lat-lon grid of 0.25 degrees for reanalysis and 0.5 degrees for uncertainty estimation. There are four main subsets: hourly and monthly products, both on pressure levels (upper air fields) and single levels (atmospheric, ocean wave and land surface quantities). These data are available via the link (copernicus.eu).

In this work to analyze the behavior of the irradiation and the cloudiness we use the EOF. This method is used by many researchers (Julianto et al., 2021; Sy et al., 2018; Munagapati & Tiwari, 2021). In climatology, the EOF (Empirical Orthogonal Function) is very often used to analyze data. We try to find temporal frequencies explaining a large percentage of the variability of a given parameter over large geographical areas. EOF analysis determines a set of functions that characterize time series covariability for a set of grid points.

If we take a discrete signal Q_i^j with Q the zero time average derivation with respect to $\overline{Q}$ and is known at points X_i with $i \in [1, N]$, at times t_j with $j \in [1, M]$. Let Q be a time series map of geopotential maps at a pressure p.

Conventions: the repetition of a subscript in an expression indicates, unless otherwise specified, a summation with respect to this subscript.

A subscript not mentioned for an array indicates a vector or a matrix. For example $Q_i \in \mathbb{R}^M$, $Q^j \in \mathbb{R}^N$, $Q \in \mathbb{R}^M \times \mathbb{R}^N$.

We define the covariance matrix by:

$$C_{il} = \frac{1}{M} Q_i^j Q_l^j = \frac{1}{M} {}^T Q_i Q_l = \overline{Q_i, Q_l}$$

The average $\overline{f, g}$ can be considered as a temporal scalar product. C is an $N \times N$, symmetric, real, positive-definite matrix. This last property appears by the fact that for all $X \in \mathbb{R}^N$.

$$ {}^T X C_{il} X_l = X_i C_{il} X_l = \frac{1}{M} X_i Q_i^j Q_l^j X_l = {}^T X {}^T Q^j Q^j X > 0 $$

Therefore, the eigenvalues of C are real and positive, arranged in decreasing order $\lambda_1 > \lambda_2 > \cdots > \lambda_N$. We assumed here that the eigenvalues are all different, which is the generic case. The associated eigenvectors $E_m \in R^N$ with components $E_{m,l}$ are the empirical orthogonal functions (EOF) for Q. Each EOF is a map in physical space for the quantity q represented by Q (for example the geopotential). The EOF E_m satisfied

$$CE_m = \lambda_m E_m \quad \text{ou} \quad C_{il} E_{m,l} = \lambda_m E_{m,i}$$

The EOF are orthogonal and can be chosen normed for the norm defined by

$$\langle X, Y \rangle = TXy = X_i Y_i$$

For $X, Y \in \mathbb{R}^N$. So we have

$$\langle E_m, E_n \rangle = \delta_{n,m}$$

We define the principal components of Q as the decomposition of the signal described by Q on the EOF E_m. We thus have

$$P_n^j = Q_i^j E_{n,i} = \langle Q^j, E_n \rangle$$

such as $Q_i^j = P_n^j E_{n,i}$ or $Q_i^j = P_n^j E_n$. The principal component $P_n \in \mathbb{R}^M$ is the coefficient of the EOF E_n and depends on time (index j) while E_n is independent of time. Similarly, $P^j \in \mathbb{R}^N$ represents the set of coefficients at time t_j. The quite remarkable property of the principal components is that they are orthogonal to each other for the norm associated with the time mean. In effect

$$\overline{P_n, P_m} = \frac{1}{M} Q_i^j E_{n,i} Q_l^j E_{m,l} = E_{n,i} C_{il} E_{m,l} = E_{n,i} \lambda_m E_{m,i} = \lambda_m \langle E_n, E_m \rangle = \lambda_m \delta_{n,m}$$

We have thus obtained a decomposition of Q in the form

$$Q = P_n E_m$$

with the double property of orthogonality

$$\langle E_n, E_m \rangle = \delta_{n,m}$$
$$\overline{P_n, P_m} = \lambda_n \delta_{n,m}$$

The fact that λ_m is the mean $\overline{P_n, P_m}$ (without summation) has a special meaning.

$$Q_i^j Q_i^j = P_n^j E_{n,i} P_n^j E_{n,i} = P_n^j P_n^j = \sum_m \lambda_m$$

The calculation of the variance makes it appear as the sum of the λ_m. As a result, we can consider $\lambda_m / \sum_n \lambda_n$ as the part of the variance associated with the EOF m.
EOF analysis was introduced in meteorology by (Lorenz, 1956). This method

has been listed many times and has different names depending on the domain (Monahan et al., 2009). In physics, it is referred to as the Karhunen-Loeve decomposition. The analysis presented here is well suited to the study of the stationary properties of variability. EOF analysis is a data reduction method that provides a compact description of the spatial and temporal variability of a data series in terms of orthogonal functions (or EOF modes) of which the former usually explain most of the variance. Its basic principle consists in decomposing each climatic variable in the form.

$$F(x,t) = \sum_{i=1}^{\infty} \alpha_i g_i(t) f_i(x)$$

where f_i and g_i are respectively spatial and temporal orthogonal functions obtained by diagonalization of the covariance matrix. In this work we evolve in a finite space therefore the function $F(x,t)$ tends to a finite value.

Frequency analysis but does not allow temporal localization of abrupt changes. The history of wavelet analysis began with Alfred Haar in 1909, Dennis Gabor (Gabor, 1946), Jean Morlet and Alex Grossmann (1984), Yves Meyer (Abel Prize 2017), Stéphane Mallat (1986), Ingrid Daubechies (1987), recognized as the founders of wavelet theory. A wavelet is an oscillating function with zero mean, denoted ψ, possessing a certain degree of regularity and whose support is finite. The mother wavelet ψ generates a family of wavelets given by (Antoine, 2018):

$$\left\{ \psi_{u,s}(t) = \frac{1}{\sqrt{s}} \psi\left(\frac{t-u}{s}\right) \right\}_{(u,s) \in \mathbb{R} \times \mathbb{R}_0^+}$$

u: time parameter (delay)

s: scale parameter

$\psi_{u,s}$: mother wavelet

ψ: translated from u and dilated

$\frac{1}{\sqrt{s}}$: multiplier coefficient

It is important to note that all irradiance and cloudiness data are taken from ERA5 and all AOD data are taken from Aeronet.

3. Results and Discussion

By studying overcast solar radiation (taken from ERA5, which is the amount of short-wavelength radiation that reaches a horizontal plane on the Earth's surface, assuming cloudless sky conditions) in the band 10 - 20. Figure 1 shows the first three EOFs of the descending clear-sky solar radiation flux in the 10 - 20 band. The special modes of the radiation flux variation extend over the entire continental shelf in the 10 - 20 band. The first two modes express 94.3% and 4.4% of the variation of solar radiation in the case of a clear sky. There is a significant transmission of the solar flux, synonymous in particular with a strong temperature gradient in the 10 - 20 band. As for the third mode, it only expresses 0.7% of the flux variation. The temporal variability of the radiant in the clear sky is given by Figure 2 with a seasonality of the covered months given by the first mode.
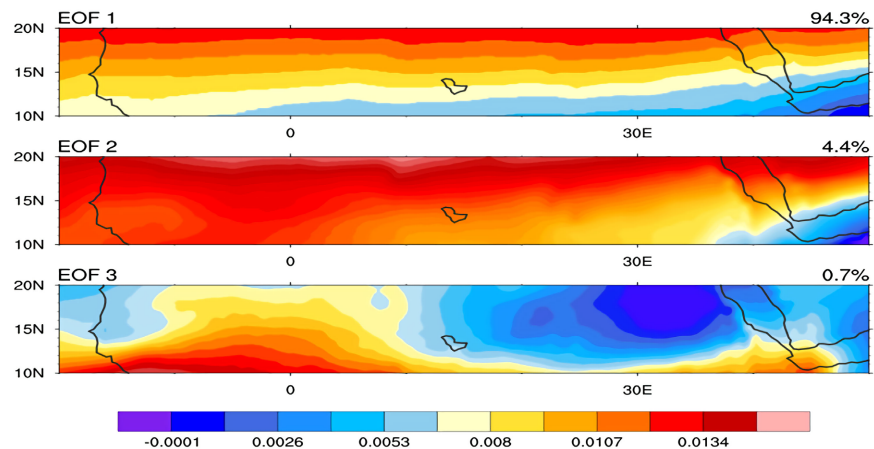
Figure 1. EOF of the spatial variation of descending solar radiation in clear sky from 1980 to 2010 in the 10 - 20 band. EOF 1 gives the first mode of the spatial variation, EOF 2 gives the second mode and EFO 3 the third mode.

For downgoing solar radiation in an overcast sky is the equivalent of what would be measured by a pyranometer at the surface of the ground in the 10 - 20 band. **Figure 3** represents the first three EOFs of the downward solar radiation flux in cloudy skies grouping both the diffuse and the direct in the 10 - 20 band. The first two modes express 65.7% and 26.2% of the variation of solar radiation, in the case of any sky. In this case, part of the solar flux is absorbed by the particles suspended in the atmosphere.

In the first two modes, between 15° North and 20° North, there is a strong solar flux. A relatively visible demarcation line is observed at 15° North. Between 10° and 15° North the solar flux seems to be more attenuated.

The third mode (**Figure 3**) expresses 2.3% of the variation of the downward solar radiation flux in cloudy skies, and reveals a maximum radiation profile between 20°West and 30°East in the 10 - 20 band.

The temporal variation observed in **Figure 4(a)** and **Figure 4(b)** highlights a seasonality of the solar flux with maxima noted in February, March, April, May, for the first mode. For the second mode the maxima are noted in the months of May, June, July and August. The third mode highlights the maximum flow profile almost in the entire 10 - 20 band. It indicates a distribution of maximum radiation minus period.

For the high cloud cover in the 10 - 20 band (high cloud at 450 hPa about 6 km) we have **Figure 5** which gives the first three modes of the EOF in the 10 - 20 band. The first mode expresses 54.5% of the cloud cover variation at 450hPa, with a weak presence noted between 15° and 20° North. A more important presence is noted as one descends towards 10° North with strong accumulations observed towards Guinea above Lake Chad and above the White Nile and Blue Nile in the South-East of Sudan.

The second mode expresses 13.6% of the variation of the high cloud cover in the 10 - 20 band, there is a strong cloud presence in the center of the band at about 15° North-20° East. These clouds are spreading westward and strengthening.
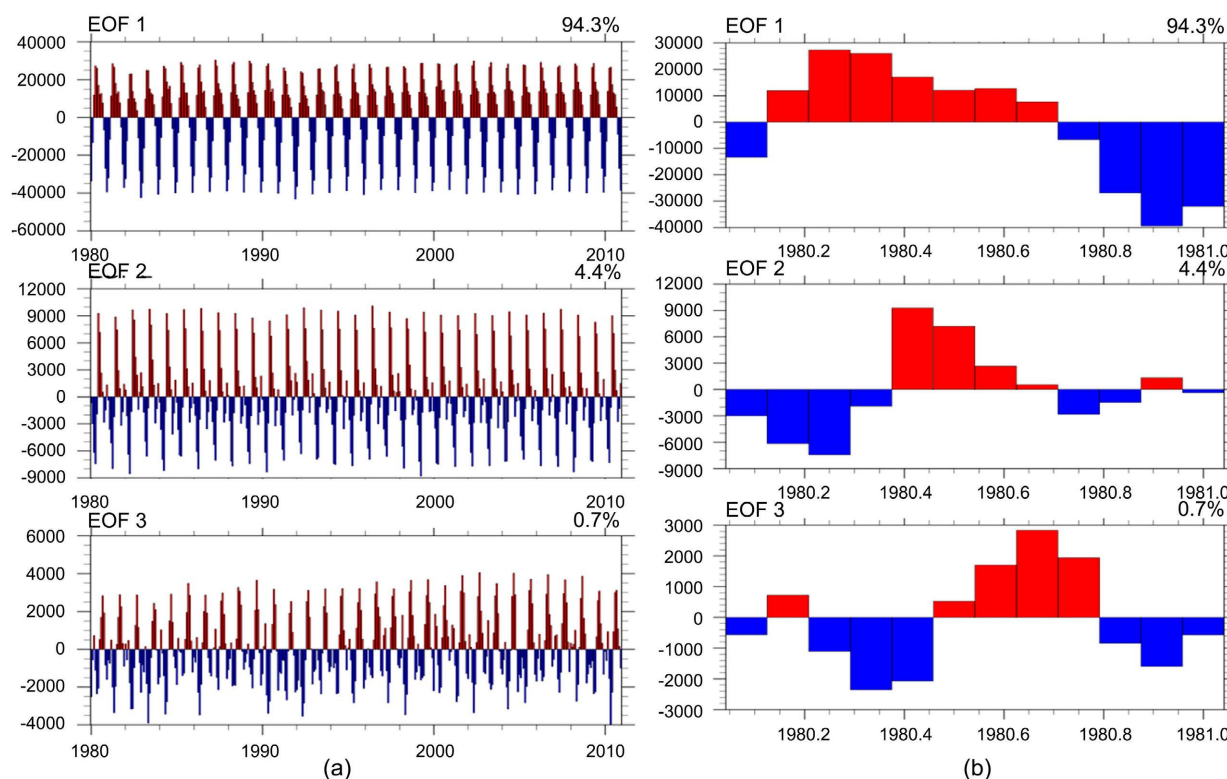
Figure 2. EOF of the temporal variation of descending solar radiation in clear sky from 1980 to 2010 in the 10 - 20 band. EOF 1 gives the first mode of the variation, EOF 2 gives the second mode and EFO 3 the third mode. (a) on the left gives the temporal variation from 1980 to 2010, (b) on the right zooms the temporal variation over one year.
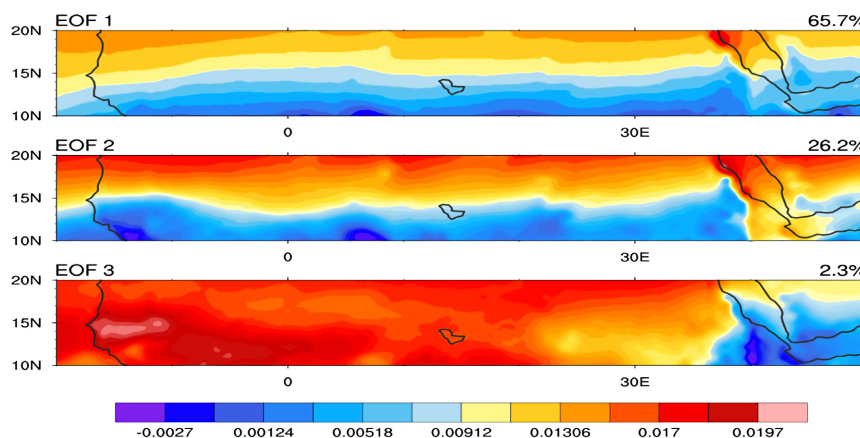

Figure 3. EOF of the spatial variation of surface solar radiation descending in overcast skies from 1980 to 2010 in the 10 - 20 band. EOF 1 gives the first mode of the spatial variation, EOF 2 gives the second mode and EFO 3 the third mode.

The third mode expresses 7.4% of the variation and highlights strong cloudiness over Guinea spreading southwest. Moderately dense cover on the border between Ethiopia and Sudan also spread towards the South-West.

Figure 6(a) and **Figure 6(b)** give the temporal variability noted in the first mode. It is relatively periodic with strong coverage noted from March to September, with maximum values in the months of May, June and July.
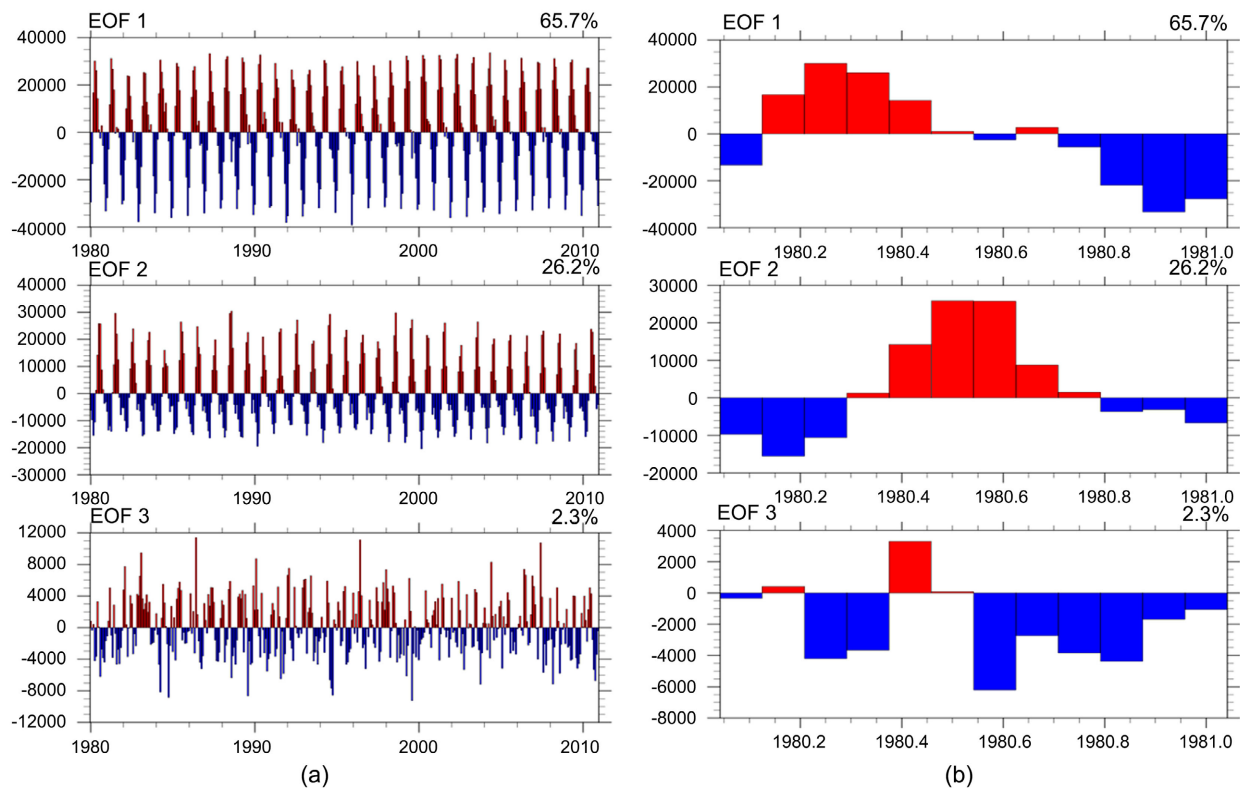
Figure 4. EOF of the temporal variation of descending solar radiation in overcast skies from 1980 to 2010 in the 10 - 20 band. EOF 1 gives the first mode of the variation, EOF 2 gives the second mode and EFO 3 the third mode. (a) on the left gives the temporal variation from 1980 to 2010, (b) on the right zooms the temporal variation over one year.
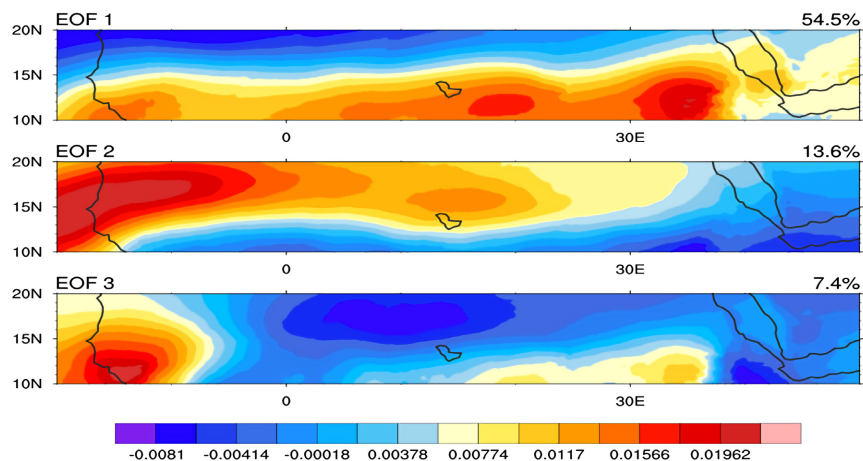

Figure 5. EOF of the spatial variation of high cloud cover from 1980 to 2010 in the 10 - 20 band. EOF 1 gives the first mode of the spatial variation, EOF 2 gives the second mode and EFO 3 the third mode.

The second and the third mode have practically no periodicity unlike the first mode.

The average cloud cover is composed of medium clouds located between about 2 km and 6 km) in the 10 - 20 band. **Figure 7** gives the first three EOFs of the average cloud cover between 800 and 450 hPa.
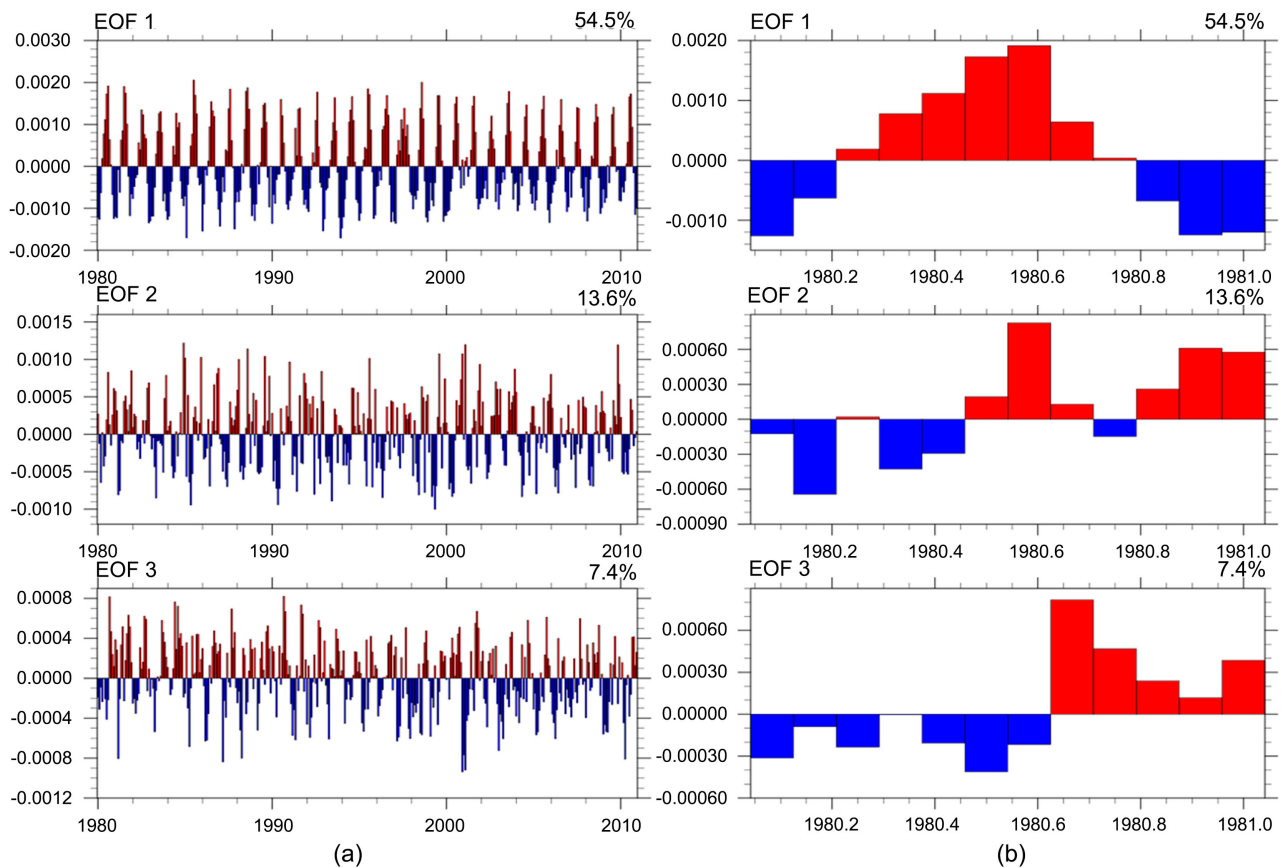
Figure 6. EOF of the temporal variation of high cloud cover from 1980 to 2010 in the 10 - 20 band. EOF 1 gives the first mode of the variation, EOF 2 gives the second mode and EFO 3 the third mode. (a) on the left gives the temporal variation from 1980 to 2010, (b) on the right zooms the temporal variation over one year.
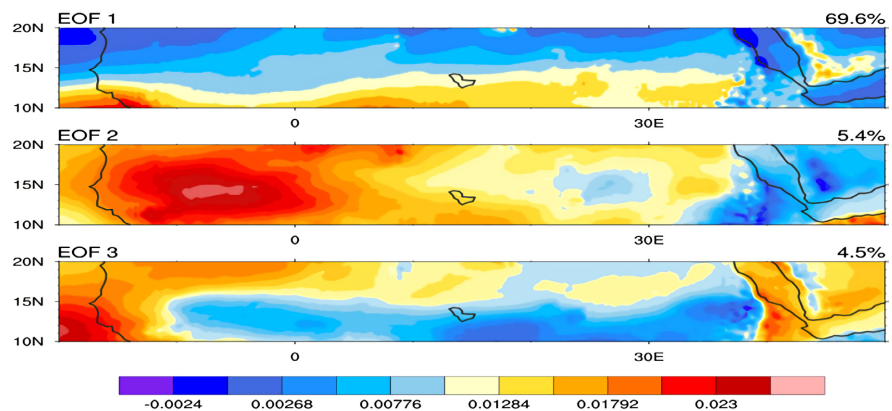

Figure 7. EOF of the spatial variation of average cloud cover from 1980 to 2010 in the 10 - 20 band. EOF 1 gives the first mode of the spatial variation, EOF 2 gives the second mode and EFO 3 the third mode.

The first mode expresses 69.6% of the variation of the mean cloud cover and shows a low amplitude of the latter in the 10 - 20 band. This variation increases slightly in the southern part of the strip, particularly towards Guinea and the northern part of Nigeria.

The second and third modes express respectively 5.4% and 4.5% of the variation of the mean cloud cover. A higher concentration is noted for these two modes in the western half of the 10 - 20 band.

Figure 8(a) shows seasonality in the first mode. With the months covered given by Figure 8(b).

10 - 20 that we note in Figure 9. We notice relatively similar profiles compared to the first three modes of the EOF of the variation of the low cloud cover in the band 10 - 20. There is a more or less significant variation in the South South-West part of the strip towards Guinea, the South of Mali, Burkina, the Niger-Nigeria border.

The first mode, which expresses 76.6% of the variation, presents an interannual seasonality with the greatest variability noted in the months of May, July, August and September (Figure 10(b)).

The second and third modes express respectively 10.8% and 2.4% and do not show any significant seasonality (Figure 10(a)).

For total cloud cover in the 10 - 20 band, Figure 11 gives the first three EOF modes of total cloud cover variation in the 10 - 20 band. With a first mode
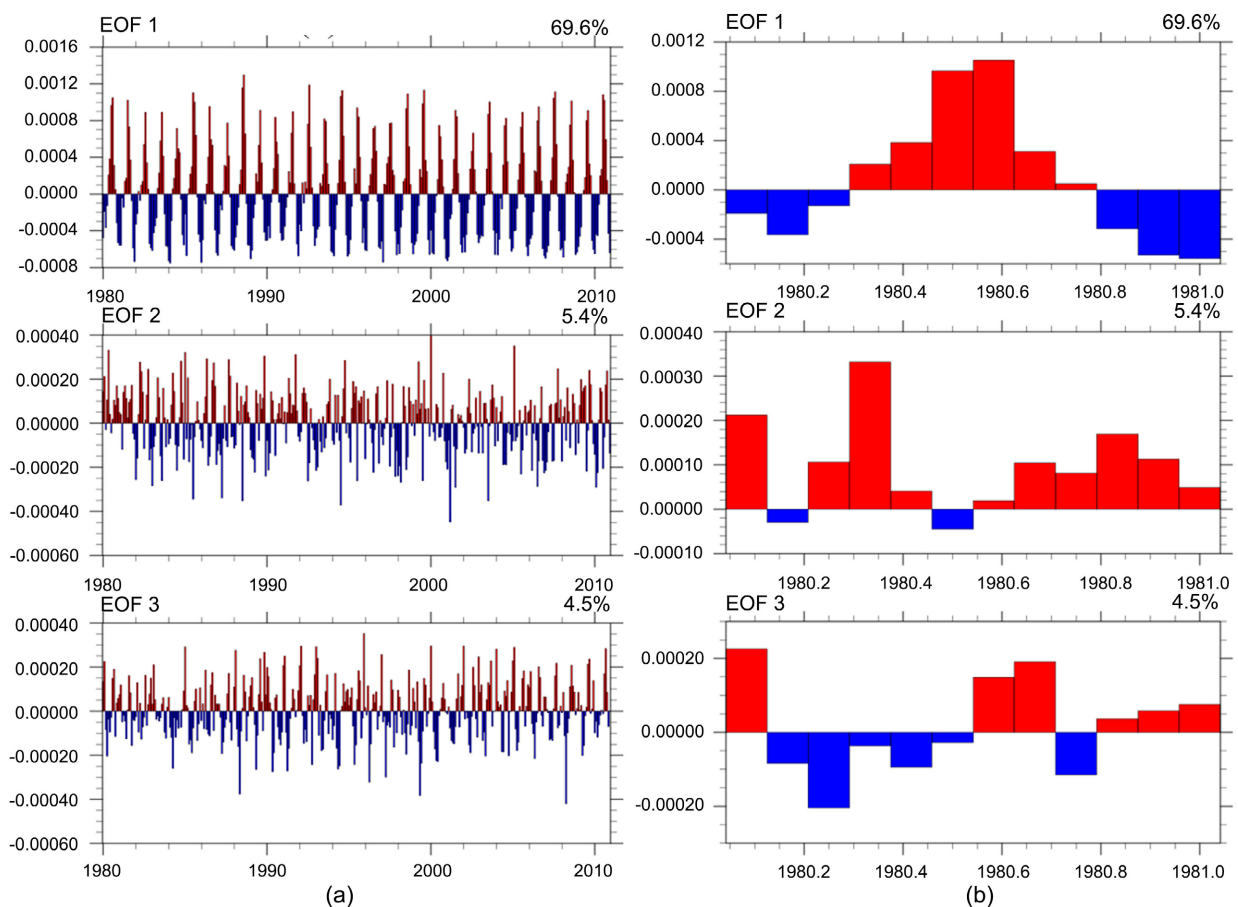

Figure 8. EOF of the variation in average cloud cover from 1980 to 2010 in the 10 - 20 band. EOF 1 gives the first mode of the variation, EOF 2 gives the second mode and EFO 3 the third mode. (a) on the left gives the temporal variation from 1980 to 2010, (b) on the right zooms the temporal variation over one year.
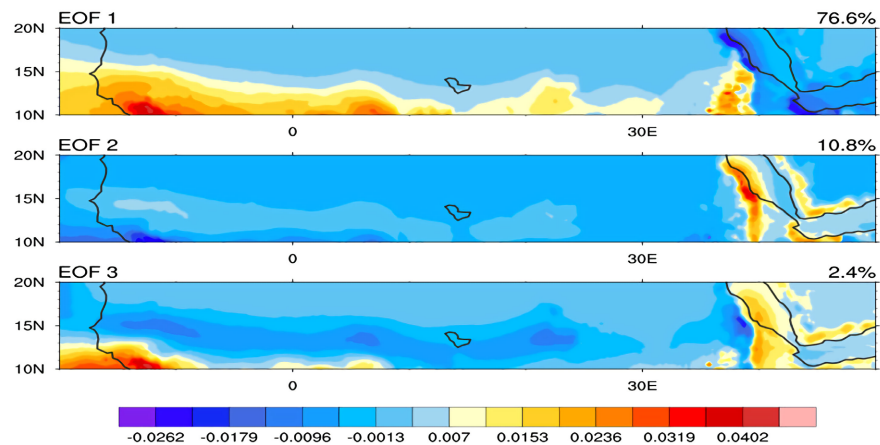
Figure 9. EOF of the spatial variation of low cloud cover from 1980 to 2010 in the 10 - 20 band. EOF 1 gives the first mode of the spatial variation, EOF 2 gives the second mode and EFO 3 the third mode.
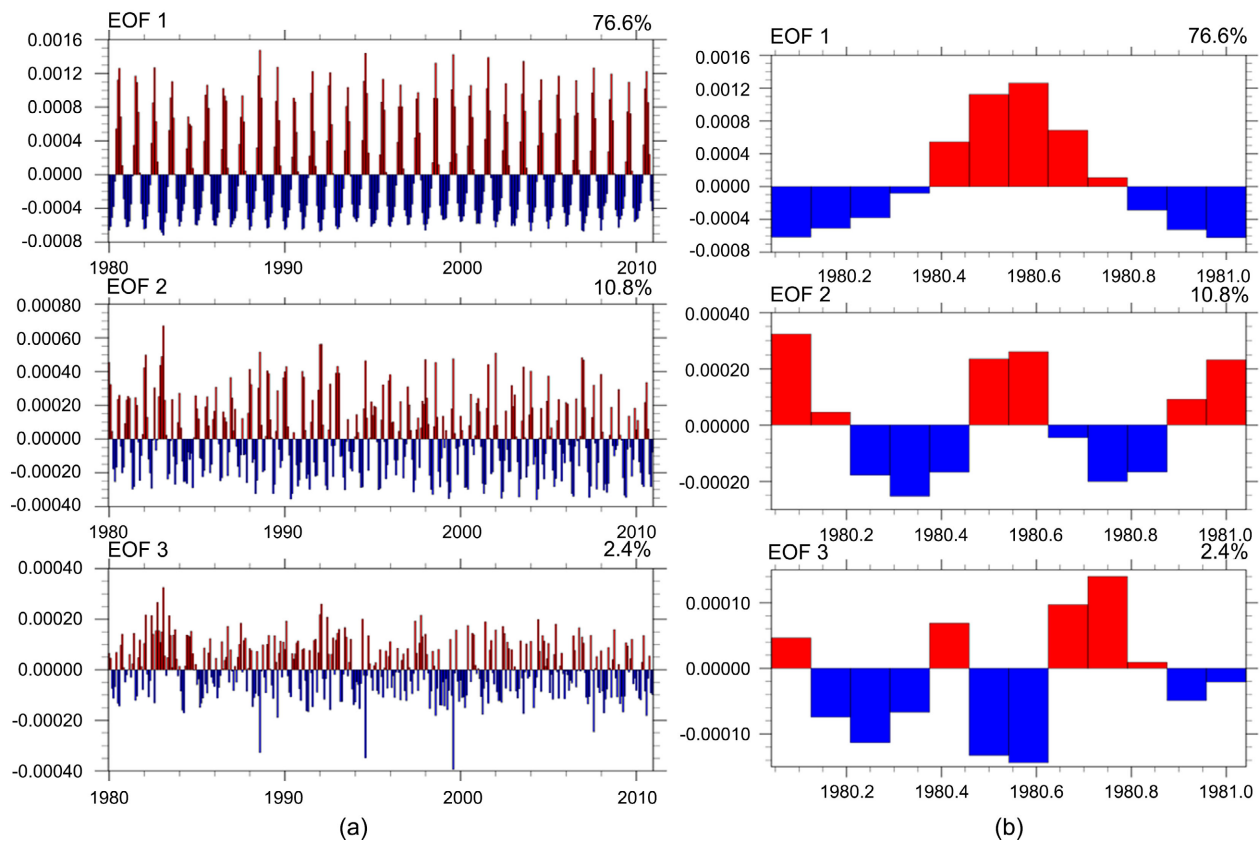

Figure 10. EOF of the variation in low cloud cover from 1980 to 2010 in the 10 - 20 band. EOF 1 gives the first mode of the variation, EOF 2 gives the second mode and EFO 3 the third mode. (a) on the left gives the temporal variation from 1980 to 2010, (b) on the right zooms the temporal variation over one year.

representing 61.4% variation, between 10° North and 15° North there is a high variability of the total cloud cover. Coverage decreases between 15° North and 20° North. A seasonality is observed (**Figure 12(a)**) from March to August, for a maximum of total coverage in June and July (**Figure 12(b)**).
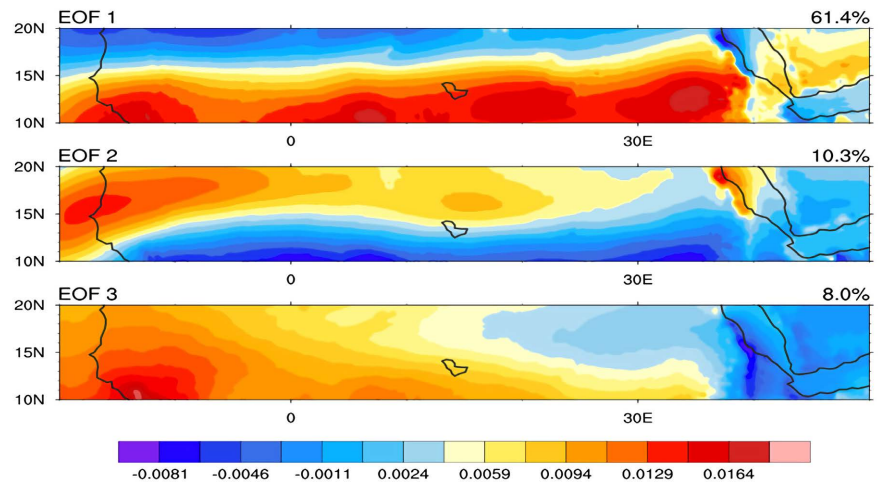
Figure 11. EOF of the spatial variation of total cloud cover from 1980 to 2010 in the 10 - 20 band. EOF 1 gives the first mode of the spatial variation, EOF 2 gives the second mode and EFO 3 the third mode.
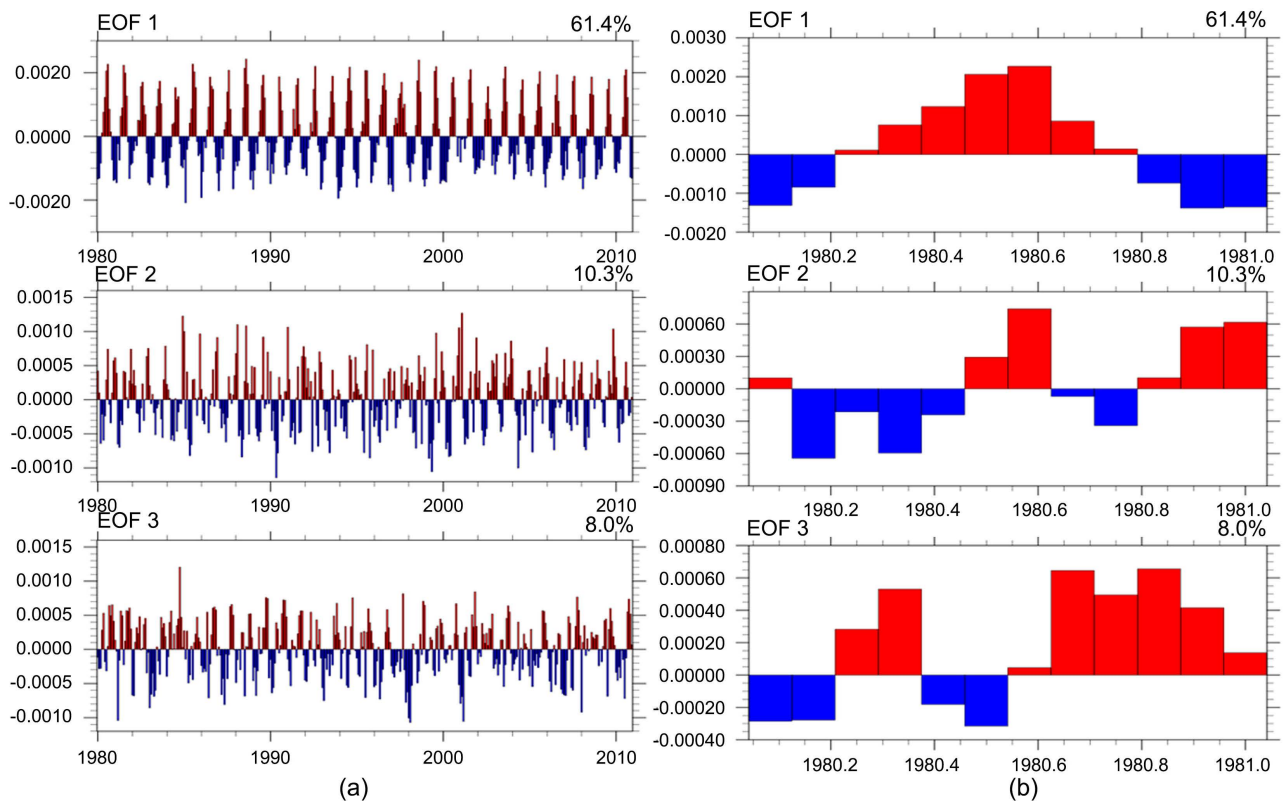

Figure 12. EOF of the change in total cloud cover from 1980 to 2010 in the 10 - 20 band. EOF 1 gives the first mode of the variation, EOF 2 gives the second mode and EFO 3 the third mode. (a) on the left gives the temporal variation from 1980 to 2010, (b) on the right zooms the temporal variation over one year.

The second and third mode express respectively 10.3% and 8% of the variability of the total cloud cover, with a strong variation observed towards the North, maxima at the level of the north coast of Senegal for the second mode, and a variation of the greater coverage towards the South South-West for the third

mode.

There is sunshine ranging from February to solar June in this area, accompanied by relatively low cloud cover, with the EOF analysis of irradiation and cloudiness in the 10 - 20 band. Hence the good capacity of this area to accommodate photovoltaic solar collectors. However, intense dust episodes were observed in this band. The study made on the AOD in the 10 - 20 band is done using wavelets.

Figure 13 and Figure 14 illustrate the average spectrum of wavelets averaged over the period 1997 to 2019 of the AODs in the Dakar station on the wavelength 440 nm and 675 nm. It can be seen that the greatest annual oscillations are observed between 1997-1998, between 2005-2006, then 2009-2010. Other optical depth variations are noted for the Dakar station. Less intense but just as significant variations are observed between 2004-2005, in 2007, at the end of 2012, between 2014 and 2015, then between 2016 and 2017. Traces of the presence of optical depth and therefore the presence of low quantity dust are noted throughout throughout the period except between 1998 and 2000.

Figure 15 and Figure 16 also illustrate the average wavelet spectrum averaged over the period 1997 to 2019 of the AODs in the Banizoumbou station on the 440 nm and 675 nm wavelengths. It can be seen that the greatest annual oscillations are observed between 2003-2004, between 2006-2007, then 2014-2015. Less intense but just as significant variations between 1997-1998, 1999-2000 and 2000-2001. Two significant average peaks are noted between 2004-2006 and 2008-2012.
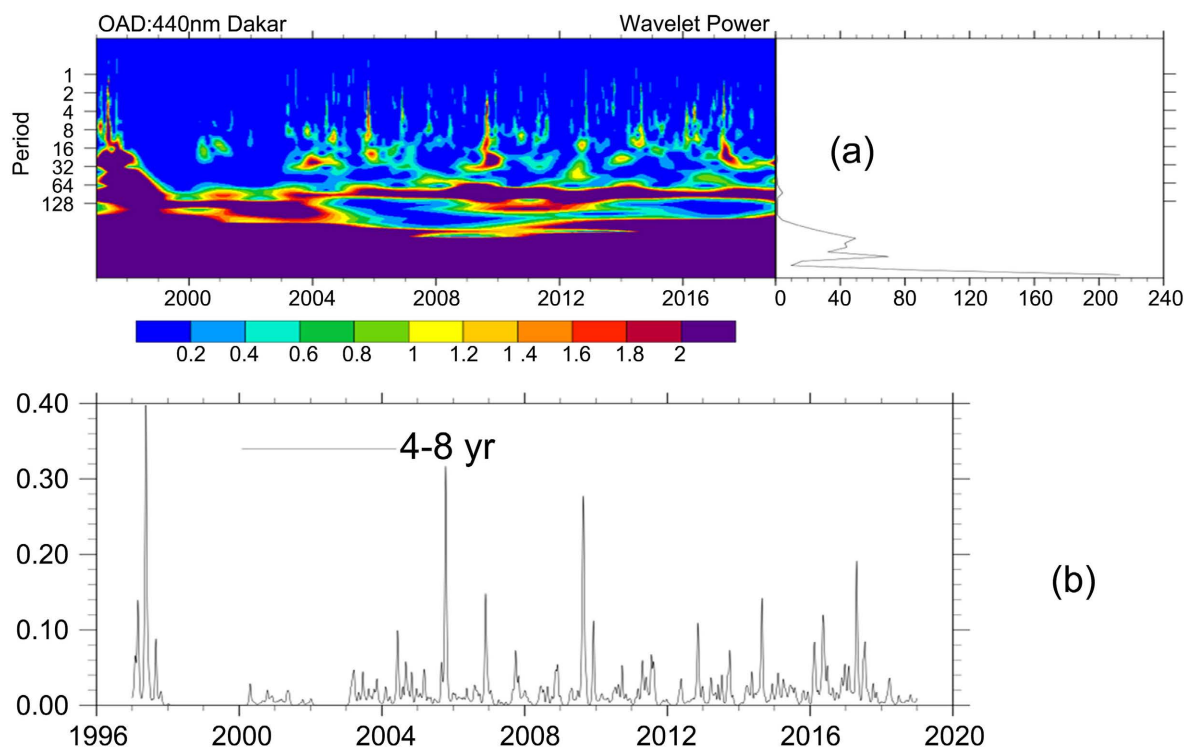

Figure 13. Wavelets associated with the 440 nm OAD in the Dakar region from 1997 to 2019. (a) gives a spectral observation of the power of the wavelets. (b) is the dust peak diagram associated with the AOD wavelets.

Figure 14. Wavelets associated with the OAD 675 nm in the Dakar region from 1997 to 2019. (a) gives a spectral observation of the power of the wavelets. (b) is the dust peak diagram associated with the AOD wavelets.
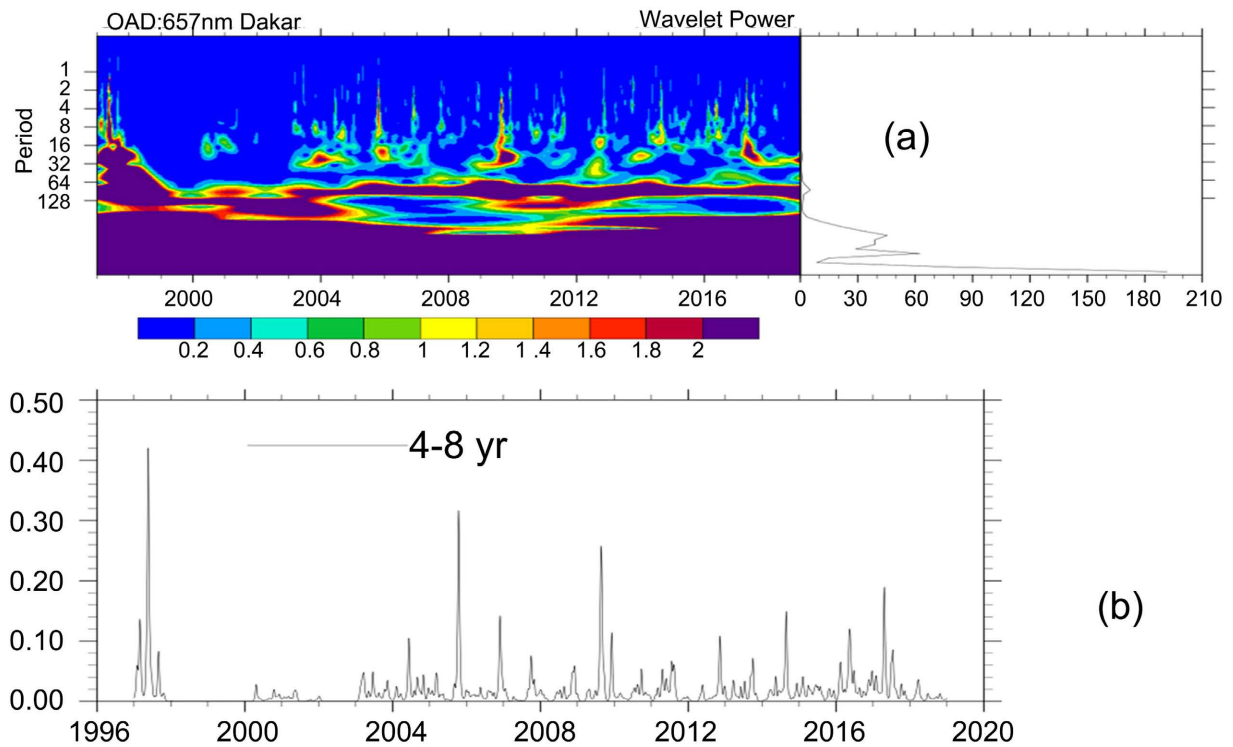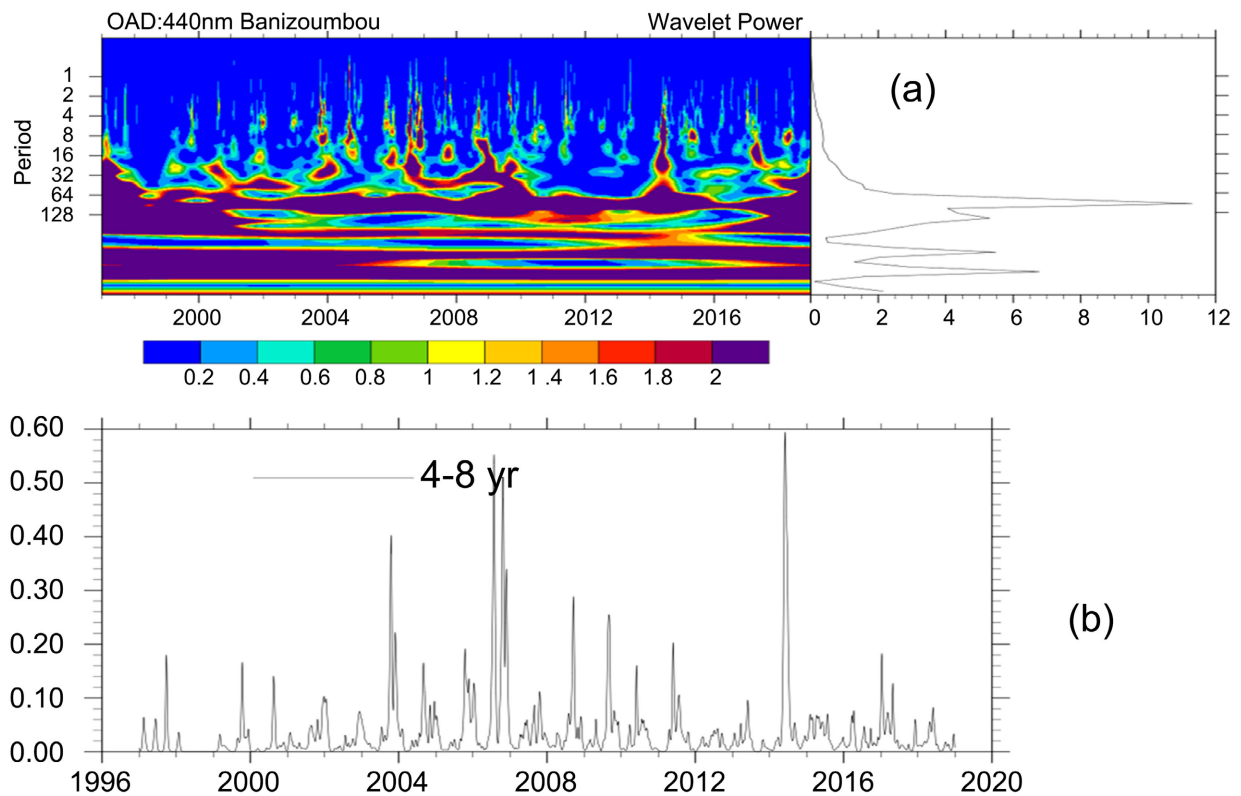

Figure 15. Wavelets associated with the OAD 440 nm in the Banizoumbou region from 1997 to 2019. (a) gives a spectral observation of the wavelet power. (b) is the dust peak diagram associated with the AOD wavelets.
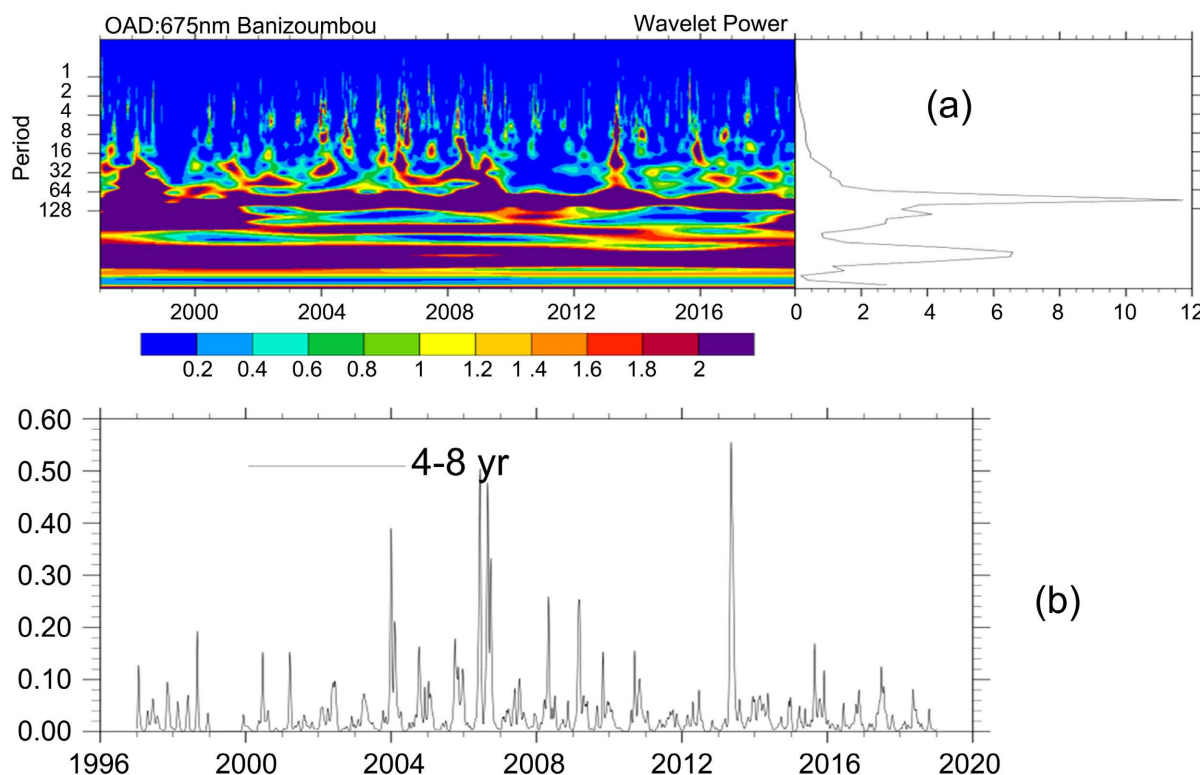
Figure 16. Wavelets associated with the OAD 675 nm in the Banizoumbou region from 1997 to 2019. (a) gives a spectral observation of wavelet power. (b) is the dust peak diagram associated with the AOD wavelets.

Three other low amplitude peaks between 2015-2016 and 2017-2018 are observed. Traces of the presence of dust are also detected throughout the period except between 1997-2000 and between 2002-2003 for Banizoumbou.

The wavelet analysis in the different stations highlights a significant presence of dust in our study area. In Banizoumbou as in Dakar the important values of optical thickness. Knowing that an aerosol optical thickness measurement characteristic of a clear sky is of the order of 0.1. A very clear sky can have an optical thickness in green light of the order of 0.05 see below. A very hazy sky gives us an aerosol optical thickness of 0.5 or more. For a particular wavelength, which crosses the atmosphere, with a sun at its zenith. For an optical thickness of 0.10, the light transmission is about 90.5%, at 0.5 the transmission is 60.7%, at 1 it is 36.8%. Knowing that on Dakar and Banizoumbou optical depth values that exceed 2 are observed. Thus, it is estimated that a study of the impact of aerosols on photovoltaic productivity in this area is necessary.

4. Conclusion

In the 10 - 20 band, the variation of solar radiation in the case of a clear sky is associated with a significant transmission of the solar flux, synonymous in particular with a strong temperature gradient. In overcast skies between 15˚ North and 20˚ North a strong solar flux is observed. This flow decreases between 10˚ and 15˚ North. The cloud cover at 450 hPa is associated with a strong cumula-

tion observed towards Guinea over Lake Chad, over the White Nile and Blue Nile in southeastern Sudan. The average coverage intensifies slightly in the southern part of the band, in particular towards Guinea and the northern part of Nigeria. There is a more or less significant variation in the low cloud cover in the south-southwest part of the band towards Guinea, southern Mali, Burkina, the Niger-Nigeria border. The total cloud cover as for it presents between 10° North and 15° North a strong variability which decreases between 15° North and 20° North. The study on the empirical orthogonal functions applied to the different types of irradiations and to the nebulosity on the different levels of pressure of the atmosphere revealed a seasonality of the latter. The wavelet analysis highlights the presence of dust in Senegal and Chad throughout the years from 1997 to 2019.

Acknowledgements

Conflicts of Interest

The authors declare no conflicts of interest regarding the publication of this paper.

References

Antoine, J.-P. (2018). Wavelet Analysis. From Oil Exploration to Relics of the Big Bang. *Review of Scientific Questions, 178,* 367-410.

deMenocal, P., Ortiz, J., Guilderson, T., et al. (2000). Abrupt Onset and Termination of the African Humid Period: Rapid Climate Responses to Gradual Insolation Forcing. *Quaternary Science Reviews, 19,* 347-361. https://doi.org/10.1016/S0277-3791(99)00081-5

Deremble, B. (2010). *Low Frequency Atmospheric Dynamics: Influence of an Ocean Temperature Front*. Thesis, Pierre and Marie Curie Sorbonne University Paris 6, Paris. https://www.theses.fr/2010PA066277

Diawara, H., Berthe, T., Bengaly, S., Gaidukova, E. V., Sangare, K., & Diarra, S. (2021). Impact of Climate Change on the Water Balance of the Sankarani River Basin in West Africa. *International Journal of Environment, Agriculture and Biotechnology, 6,* 119-126. https://doi.org/10.22161/ijeab.66.14

Emeterio, J.-L. S., Lacaze, B., & Méring, C. (2012). Detection of Vegetation Cover Changes in the Sahel during the Period 1982-2002 from NDVI and Precipitation Data. *Remote Sensing Review, 10,* 2-3.

Gabor, D. (1946). Theory of Communication: Part 1: The Analysis of Information. *Journal of the Institute of Electrical Engineering, 93,* 429-457. https://doi.org/10.1049/ji-3-2.1946.0074

Julianto, M. T., Dhimas, S., Sopaheluwakan, A., Nurdiati, S., & Septiawan, P. (2021). Identification of Global Warming Contribution to the El Niño Phenomenon Using Empirical Orthogonal Function Analysis. *Agromet, 35,* 11-19. https://doi.org/10.29244/j.agromet.35.1.11-19

Lorenz, E. N. (1956). *Empirical Orthogonal Functions and Statistical Weather Prediction.*

Statistical Forecasting Project Rep. 1, MIT Department of Meteorology, 49.

Marega, O., Emeterio, J.-L. S., Fall, A., & Andrieu, J. (2021). Remote Sensing Mapping of Vegetation Land Cover Change with Regard to Rainfall Variability in the Sahel: A Multiscale Approach. *Physio-Géo, 16,* 1-28. https://doi.org/10.4000/physio-geo.11977

Martiny, N., Roucou, P., & Adde, A. (2014). Impact of Climate on Health: Regional Dust Modeling for Meningitis Epidemics in the Sahel. *27th Colloquium of the International Association of Climatology*, Dijon, July 2014, 657-662.

Monahan, A., Fyfe, J. C., Ambaum, M. H. P., Stephenson, D. B., & North, G. R. (2009). Empirical Orthogonal Functions: The Medium is the Message. *Journal of Climate, 22,* 6501-6514. https://doi.org/10.1175/2009JCLI3062.1

Munagapati, H., & Tiwari, V. M. (2021). Spatio-Temporal Patterns of Mass Changes in Himalayan Glaciated Region from EOF Analyses of GRACE Data. *Remote Sensing, 13,* 265. https://doi.org/10.3390/rs13020265

Nouaceur, & Zeineddine. (2020). Rain Resumption and Floods Multiplication in Western Sahelian Africa. *Physio-Géo, 15,* 89-109.

Nouaceur, Z. (2004). Haze, Dust Haze, Dust Blower and Sandstorm Specific Types of Weather in Dry Regions. *Brume sèche, brume de poussière, chasse-sable et tempête de sable. Des types de temps spécifiques des régions sèches, 2,* 11.

Olauson, J. (2018). ERA5: The New Champion of Wind Power Modelling? *Renewable Energy, 126,* 322-331. https://doi.org/10.1016/j.renene.2018.03.056

Paturel, J. E., Servat, E., Delatre, M. O., & Lubes-niel, H. (1998). Analysis of Rainfall Long Series in Non-Sahelian West and Central Africa within a Context of Climate Variability. *Hydrological Sciences Journal, 43,* 937-946.

Rajot, J. L., Toure, A., Guillon, R., Zibogarba, P. C., Bichet, V., & Marticorena, B. (2011). Terrigen Dust in the Sahel—A Climatic or Anthropogenic Marker? In *Ngaoundéré (CMR): International Colloquium: Water, Climate and Environmental Sciences for Sustainable Development in Africa* (p. 50). Ngaoundere (CMR).

Sicard, B. (1992). Influences of Aridity on the Biology of Sudano-Sahelian Rodents.

Sy, A., Diop, B., Farota, A. K., Sarr, D., Dia, A., Diop, A. B., Pohl, B., & Duroure, C. (2018). Role of Indian Fluxes in the Intraseasonal 10-30 Days Variability of the African Monsoon. *Journal of Earth Science & Climatic Change, 9,* Article ID: 1000495. https://doi.org/10.4172/2157-7617.1000495

Taïbi, A. N. (2017). Desertification on Both Sides of the Largest Desert in the World. The Sahara and Its Northern and Southern Margins; A Context Favorable to Desertification? In: J. Andrieu, Ed., *Africa, from the Sahel and the Sahara, to the Mediterranean* (pp. 259-270), Desertification.

Wang, C., Graham, R. M., Wang, K., Gerland, S., & Granskog, M. A. (2019). Comparison of ERA5 and ERA-Interim Near-Surface Air Temperature, Snowfall and Precipitation over Arctic Sea Ice: Effects on Sea Ice Thermodynamics and Evolution. *The Cryosphere, 13,* 1661-1679. https://doi.org/10.5194/tc-13-1661-2019